Precipitation evolution in Al–0.1Sc, Al–0.1Zr and Al–0.1Sc–0.1Zr (at.%) alloys during isochronal aging

Keith E. Knipling [a,b,*], Richard A. Karnesky [a,c], Constance P. Lee [a], David C. Dunand [a], David N. Seidman [a,d]

[a] Department of Materials Science and Engineering, Northwestern University, Evanston, IL 60208-3108, USA
[b] US Naval Research Laboratory, Multifunctional Materials Branch, Washington, DC 20375-0001, USA
[c] Sandia National Laboratories, Livermore, CA 94550-9610, USA
[d] Northwestern University Center for Atom-Probe Tomography (NUCAPT), Evanston, IL 60208-3108, USA

Abstract

Precipitation strengthening is investigated in binary Al–0.1Sc, Al–0.1Zr and ternary Al–0.1Sc–0.1Zr (at.%) alloys aged isochronally between 200 and 600 °C. Precipitation of Al_3Sc ($L1_2$) commences between 200 and 250 °C in Al–0.1Sc, reaching a 670 MPa peak microhardness at 325 °C. For Al–0.1Zr, precipitation of Al_3Zr ($L1_2$) initiates between 350 and 375 °C, resulting in a 420 MPa peak microhardness at 425–450 °C. A pronounced synergistic effect is observed when both Sc and Zr are present. Above 325 °C, Zr additions provide a secondary strength increase from the precipitation of Zr-enriched outer shells onto the Al_3Sc precipitates, leading to a peak microhardness of 780 MPa at 400 °C for Al–0.1Sc–0.1Zr. Compositions, radii, volume fractions and number densities of the $Al_3(Sc_{1-x}Zr_x)$ precipitates are measured directly using atom-probe tomography. This information is used to quantify the observed strengthening increments, attributed to dislocation shearing of the $Al_3(Sc_{1-x}Zr_x)$ precipitates.
Published by Elsevier Ltd. on behalf of Acta Materialia Inc.

Keywords: Aluminum alloys; Precipitation; Scandium; Zirconium; Atom-probe tomography

1. Introduction

Of all alloying additions to Al, Sc and Zr offer the greatest potential for developing creep-resistant, thermally stable alloys at elevated temperatures [1]. During post-solidification aging, supersaturated Al–Sc or Al–Zr solid-solutions form nanometer-scale Al_3Sc or Al_3Zr ($L1_2$ structure) precipitates, which are coherent with the α-Al solid-solution and act as effective strengtheners at ambient and elevated temperatures. Sc is singular among all transition metal solutes because the Al_3Sc trialuminide formed has a thermodynamically stable $L1_2$ structure. Compared with other transition metals Sc has, however, a relatively large diffusivity in α-Al [1] and Al–Sc alloys are only coarsening resistant up to ~300 °C [2–8]. Zr is a much slower diffuser in α-Al, but the $L1_2$ structure of Al_3Zr is thermodynamically metastable. Nevertheless, the precipitates are kinetically stable to ~475 °C, above which the metastable $L1_2$ Al_3Zr precipitates coarsen and transform to their equilibrium $D0_{23}$ structures [9]. These Al_3Zr precipitates are, however, heterogeneously distributed because of the dendritic microsegregation of Zr atoms during solidification [10,11], and the resulting precipitate-free interdendritic channels have a deleterious effect on the mechanical properties at ambient temperature [9] and during creep [12].

In the extensively studied Al–Sc–Zr system [13] an ordered $L1_2$ $Al_3(Sc_{1-x}Zr_x)$ trialuminide is formed with up to half of the Sc atoms being replaced by Zr [14]. In precipitates formed in alloys, however, the Zr concentrations are

* Corresponding author at: US Naval Research Laboratory, Multifunctional Materials Branch, Washington, DC 20375-0001, USA.
 E-mail address: knipling@anvil.nrl.navy.mil (K.E. Knipling).
 URL: http://arc.nucapt.northwestern.edu/ (D.N. Seidman).

much smaller than this maximum value of $x = 0.5$ [15,16] because of the much smaller diffusivity of Zr in α-Al. Zr segregates at the α-Al/$Al_3(Sc_{1-x}Zr_x)$ interface, forming a Zr-rich shell surrounding a Sc-rich core [15–19]. In this article, we describe the synergistic effects obtained when equal concentrations of Sc and Zr are added to Al. As in other studies [20–22], we employ isochronal heat treatments to obtain a high number density of precipitates. We measure the mean radii ($\langle R \rangle$), volume fractions (ϕ) and number densities (N_v) of the $Al_3(Sc_{1-x}Zr_x)$ precipitates simultaneously using atom-probe tomography (APT) reconstructions, and correlate the strength predicted by using these parameters in classical precipitation-hardening models with the measured microhardness.

2. Experimental procedures

2.1. Alloy compositions and preparation

Binary Al–0.1Sc and Al–0.1Zr alloys and a ternary Al–0.1Sc–0.1Zr alloy were investigated; alloy designations and exact compositions are summarized in Table 1 (all compositions are in at.% unless otherwise noted). Small (~7 g) buttons were prepared by melting 99.95 at.% Al (Atlantic Equipment Engineers, Bergenfield, NJ) with a dilute Al–0.12Sc master alloy (Ashurst Technology, Ltd., Baltimore, MD) and/or an Al–0.57Zr master alloy, employing non-consumable electrode arc-melting in a gettered purified-argon atmosphere. The pure Al contained 260 at. ppm Fe and 260 at. ppm Si as impurities, as determined by glow-discharge mass spectrometry (Shiva Technologies/Evans Analytical Group, Syracuse, NY). The Al–0.57 Zr master alloy was dilution cast from a commercial 10 wt.% Zr master alloy (KB Alloys, Reading, PA). The verified compositions in Table 1 were obtained by bulk chemical analysis performed by direct current plasma emission spectroscopy (ATI Wah Chang, Albany, OR).

Except for the Al–Sc binary alloy, the alloys were not homogenized prior to post-solidification aging. This is because Al–Zr alloys (with sufficient Zr concentrations for appreciable precipitation strengthening) cannot be homogenized without first nucleating Al_3Zr precipitates, resulting in minimal precipitation hardening during subsequent aging [11]. The Al–Sc–Zr castings were intentionally left in their as-cast state to take advantage of the expected microsegregation of Sc at the Zr-poor dendrite peripheries. The Al–Sc alloy was studied in both the as-cast and homogenized states; homogenization was carried out at 640 °C for 28 h.

Two button ingots of Al–0.1Sc–0.1Zr, labeled (a) and (b), were prepared in order to ensure that sufficient material was available for subsequent analyses. Most analyses were performed on Al–0.1Sc–0.1Zr(a), which was only aged to 400 °C to preserve the bulk of the material in the peak-aged condition and to allow for subsequent isothermal aging. Likewise, the as-cast specimen of Al–0.1Sc was only aged to 400 °C, while the homogenized specimen was aged to 500 °C.

2.2. As-cast microstructural analysis

The microstructures of the as-cast specimens were observed by scanning electron microscopy (SEM) using a JEOL JSM-7000F microscope. The initial solute distribution was measured in as-cast specimens by quantitative electron-probe microanalysis (EPMA) using a Cameca SX50 EPMA operating at 15 kV and 20 nA, equipped with four wavelength dispersive spectrometers (WDSs). The reported uncertainty is one standard deviation of the analytical sensitivity.

2.3. Aging treatments and analytical techniques

The alloys were aged isochronally in 25 °C steps lasting 3 h each, beginning at 200 °C and terminating at 600 °C. After each aging step, the specimens were water-quenched and precipitation of Al_3Sc, Al_3Zr, or $Al_3(Sc_{1-x}Zr_x)$ was monitored by Vickers microhardness and electrical conductivity measurements. The Vickers microhardness measurements were performed at ambient temperature on metallographically polished sections using a load of 200 g and a dwell time of 5 s. A minimum of 20 hardness measurements were recorded for each temperature. The electrical conductivity measurements were performed at ambient temperature using an eddy current apparatus (Sigmatest 2.069 from Foerster Instruments, Pittsburgh, PA), placing the contact probe on a clean, planar surface. Five measurements were recorded, each corresponding to a different frequency (60, 120, 240, 480 or 960 kHz), on each specimen. For consistency, a single specimen of each alloy was used for the electrical conductivity measurements, which was recorded between each isochronal aging step. An increase in electrical conductivity corresponds to a decrease in the solute concentration in the matrix due to an increased precipitate volume fraction [23–27]. Uncertainty in both measurements is reported as one standard deviation from the mean.

The compositions, $\langle R \rangle$, ϕ and N_v values of the $Al_3(Sc_{1-x}Zr_x)$ precipitates were measured employing three-dimensional atomic reconstructions obtained using a local electrode atom-probe™(LEAP) 3000X Si tomograph [28–32]. Needle-like APT specimens were prepared by a two-step electropolishing procedure. Specimen blanks,

Table 1
Compositions of the Al–Sc, Al–Zr and Al–Sc–Zr alloys investigated (at.%).

Alloy	Nominal composition		Verified composition[a]	
	Sc	Zr	Sc	Zr
Al–0.1Sc	0.10	–	0.093	–
Al–0.1Zr	–	0.10	–	0.101
Al–0.1Sc–0.1Zr(a)	0.10	0.10	0.089	0.092
Al–0.1Sc–0.1Zr(b)	0.10	0.10	0.090	0.091

[a] As measured by direct current plasma emission spectroscopy.

excised from aged specimens and mechanically ground to approximately $0.2 \times 0.2 \times 10$ mm^3, were initially shaped into needle-like tips using a solution of 10 vol.% perchloric acid in acetic acid at ~10 V d.c. at ambient temperature. Final electropolishing involved formation of a neck near the tip apex, controlled by limiting the amount of chemical solution in contact with the area of the neck using a loop-polishing apparatus. A solution of 2 vol.% perchloric acid in butoxyethanol was employed for this final tip-sharpening procedure, with an applied potential of 3–8 V d.c. at room temperature. The resulting specimen has an end radius of curvature <50 nm. Pulsed field-evaporation was conducted under ultrahigh vacuum (UHV) conditions ($<10^{-10}$ Torr gauge pressure) at a specimen temperature of 30 K utilizing a pulse fraction (ratio of the pulse voltage to the steady-state DC imaging voltage) of 15–20% and a pulse repetition rate of 200 kHz. A fixed flight path of 80 mm was used for all analyses. Post-analysis data visualization and evaluation were performed with IVAS v. 3.4.1 (Imago Scientific Instruments, Madison, WI). Precipitates were isolated and studied quantitatively using the proximity histogram [33,34] and envelope methods [35,36], as discussed in detail below.

3. Results

3.1. As-cast microstructure

The as-cast macrostructures of the binary Al–Sc [26,37] and Al–Zr [10] alloys are typical of conventionally cast alloys, exhibiting coarse (millimeter-scale) columnar grains. The Al–Sc–Zr alloy has a much finer macrostructure, Fig. 1, consisting of equiaxed grains ~50 μm in diameter and copious precipitation of $Al_3(Sc_{1-x}Zr_x)$ primary precipitates. These primary precipitates are 3–5 μm in diameter and have a petal-like shape. This morphology is characteristic of the $L1_2$ structure of Al_3Zr (metastable) [38,39] or

Fig. 1. SEM micrograph of metallographically polished as-cast Al–0.1Sc–0.1Zr(a). The α-Al grains are fine and equiaxed (~50 μm), containing several primary $Al_3(Sc_{1-x}Zr_x)$ precipitates. The primary precipitates have a petal-shaped morphology (see inset).

Al_3Sc (equilibrium) [40–42] primary precipitates, whose cubic structure is commensurate with α-Al (fcc) and acts as an effective heterogeneous nucleant of α-Al during solidification. The primary precipitates are Zr-rich with a Zr:Sc ratio of ~3 on an at.% basis, as measured by EPMA.

3.2. As-cast solute microsegregation

The as-cast microsegregation of Sc and Zr atoms was determined by linear composition profiles measured by EPMA, Fig. 2, in two regions of the ternary alloy Al–0.1Sc–0.1Zr(a). Each 40 μm long analyzed traverse spans multiple dendritic cells in each specimen, as evidenced by the periodic variations in solute concentration. The wavelength of the variations, which presumably corresponds to the secondary dendrite arm spacing, is ~30 μm. The horizontal dashed lines indicate the mean measured solute concentrations for each set of data. The dendrites are enriched in Zr and concomitantly depleted in Sc, and vice versa for the interdendtric regions. While qualitatively similar, the degree of microsegregation in Fig. 2a and b is different, suggesting that there is a macrosegregation of solutes between the two regions sampled.

Sc atoms are concentrated in the interdendritic regions, the last solid to form. In Fig. 2a, the maximum enrichment of Sc is ~0.11 at.% (i.e. ~0.01 at.% above the measured mean composition of 0.098 ± 0.004 at.% Sc), whereas in Fig. 2b the maximum Sc concentration is ~0.13 at.% (i.e. ~0.03 at.% above the measured mean concentration of 0.099 ± 0.004 at.% Sc). Near the dendrite centers the Sc concentration is ~0.085 at.% (i.e. ~0.015 at.% below the mean) in Fig. 2a and b. Zr partitions much more strongly, varying by more than 0.05 at.% about the measured mean composition of 0.124 ± 0.012 at.% Zr in Fig. 2a. In Fig. 2b, however, the degree of Zr segregation is less pronounced and is comparable to that of Sc.

3.3. Vickers microhardness and electrical conductivity

Fig. 3 displays the precipitation behavior of Al–0.1Sc, Al–0.1Zr and Al–0.1Sc–0.1Zr during isochronal aging, as monitored by Vickers microhardness and electrical conductivity measurements. Precipitation of Al_3Sc ($L1_2$) commences between 200 and 250 °C in the binary Al–Sc alloy, as evidenced by the increase in strength and the accompanying change in electrical conductivity, achieving a peak microhardness of 668 ± 20 MPa at 325 °C. There is a continuous decrease in microhardness above 325 °C. Peak electrical conductivity, which corresponds to a maximum ϕ of Al_3Sc ($L1_2$) precipitates, is achieved at ~375 °C, which is 50 °C higher than the peak microhardness temperature. The difference in electrical conductivity between the as-cast and maximum value is 2.7 ± 0.4 MS m^{-1}. Above 400 °C, the decreasing electrical conductivity and the concomitant increased scatter in the data suggests that Al_3Sc precipitates are dissolving. By 500 °C, virtually all precipitation strengthening is lost and the Al–0.1Sc alloy has returned to its initial

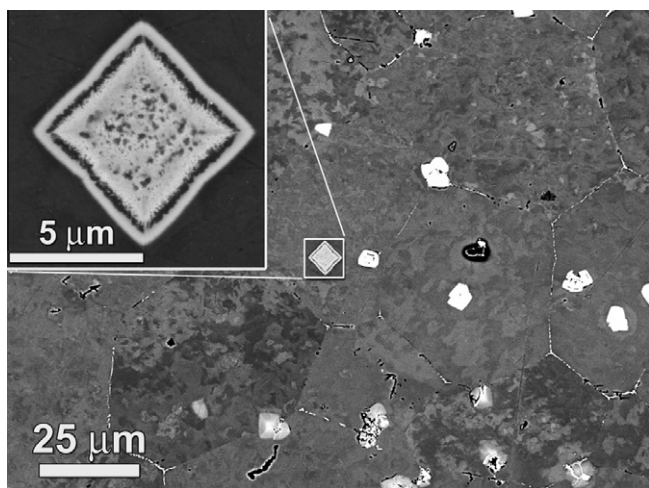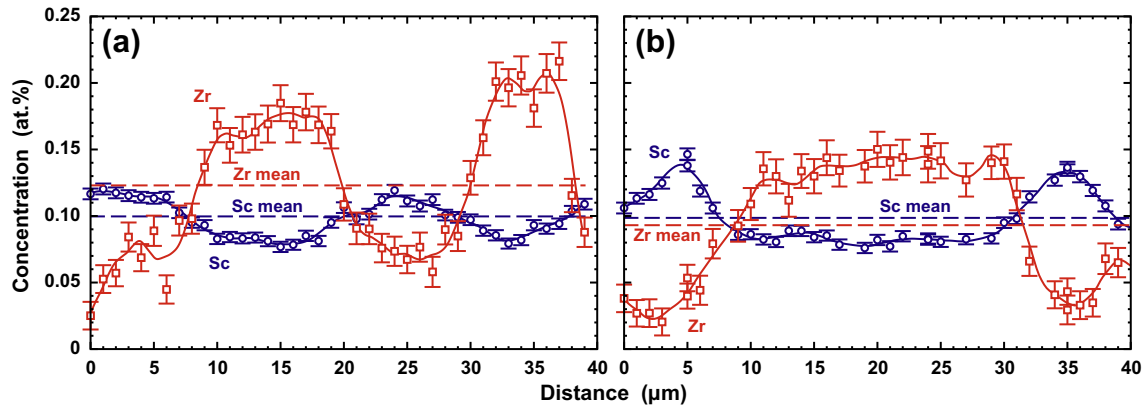Fig. 2. Concentration profiles of Sc and Zr, measured by EPMA, across multiple dendritic cells from two regions in as-cast Al–0.1Sc–0.1Zr(a). The horizontal dashed lines indicate the mean measured solute concentrations.

as-cast microhardness. Homogenizing Al–0.1Sc prior to aging has no effect on the observed microhardness or change in electrical conductivity. The systematically smaller electrical conductivity ($\sim$0.6 MS m^{-1}) for the homogenized specimen is probably due to differences in specimen geometry.

In the Al–0.1Zr alloy, precipitation of Al$_3$Zr (L1$_2$) commences between 350 and 375 °C and leads to a peak microhardness value of 420 $\pm$ 8 MPa at 425–450 °C, with a corresponding change in electrical conductivity of 3.6 $\pm$ 0.1 MS m^{-1}. Above 475 °C, there is a continuous decrease in microhardness with a concomitant decline in electrical conductivity, which is due to coarsening and dissolution of the spheroidal Al$_3$Zr (L1$_2$) precipitates and their transformation to their equilibrium D0$_{23}$ structure, as studied in detail in Ref. [9].

The as-cast electrical conductivities of Al–0.1Sc (30.5 $\pm$ 0.4 MS m^{-1}) and Al–0.1Zr (29.7 $\pm$ 0.1 MS m^{-1}) are similar and much smaller than the peak conductivities measured, implying that the specific resistivities of the two solute elements are also comparable. The electrical conductivity of as-cast Al–0.1Sc–0.1Zr (26.4 $\pm$ 0.3 MS m^{-1}) is significantly smaller than the binary alloys because the ternary alloy contains twice the nominal amount of solute as the binary alloys. The as-cast microhardness of Al–0.1Sc–0.1Zr is also $\sim$50 MPa greater than that of the binary alloys, which may be attributable to greater solid-solution strengthening and/or Hall–Petch strengthening due to the finer grain size, Fig. 1. Precipitation strengthening of Al–0.1Sc–0.1Zr is equivalent to that of Al–0.1Sc up to 325 °C, with a comparable change in electrical conductivity, suggesting that a similar ϕ of precipitates is generated in both cases. The Al–0.1Sc alloy reaches peak hardness at 325 °C, while the Al–01Sc–01Zr alloy experiences additional precipitate nucleation and growth, as evidenced by the continued increases in microhardness and electrical conductivity above 325 °C. A peak microhardness of 782 $\pm$ 37 MPa is achieved at 400 °C and peak electrical conductivity, corresponding to maximum ϕ, occurs at 475 °C. Additions of Zr delay overaging by 100–125 °C as compared with the Al–Sc alloy; note that

at 600 °C (0.94T_m) there is still a perceptible strengthening effect for the Al–Sc–Zr alloy, although the reduced electrical conductivity suggests that significant precipitate dissolution has occurred.
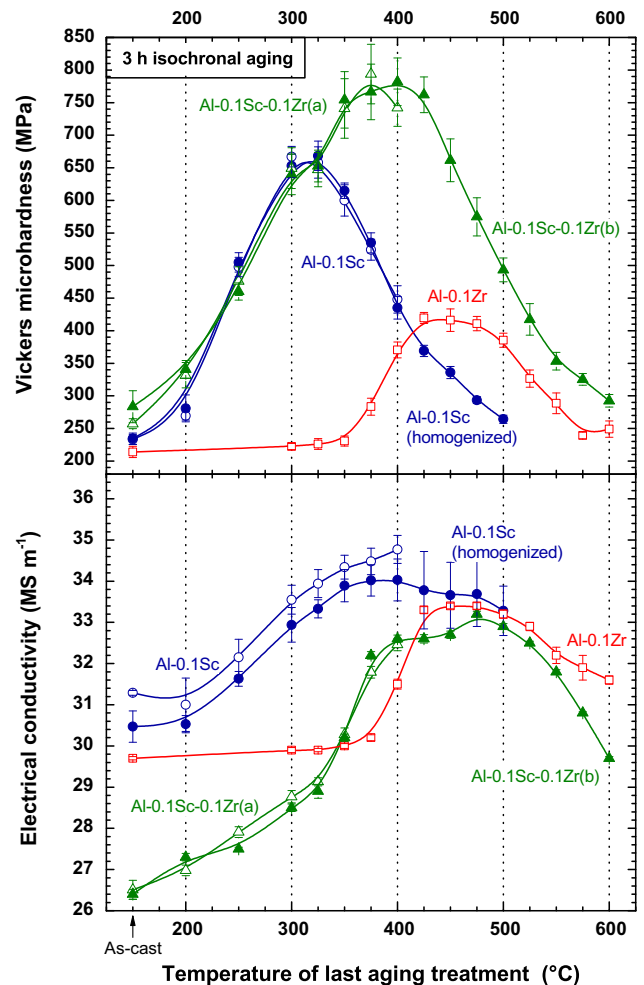

Fig. 3. Vickers microhardness and electrical conductivity evolution during isochronal aging (3 h at each temperature) of Al–0.1Zr, Al–0.1Sc and Al–0.1Sc–0.1Zr (at.%) alloys.

3.4. Atom-probe tomography

The ternary Al–0.1Sc–0.1Zr(a) alloy was investigated by APT to determine the precipitate compositions, $\langle R \rangle$, ϕ, and N_v values. Three aging temperatures of interest were selected from Fig. 3: 300 °C (before the departure from binary Al–Sc behavior), 350 °C (near-peak microhardness) and 400 °C (peak microhardness and near-peak electrical conductivity). Fig. 4 presents APT reconstructions for these isochronal aging conditions, displaying Sc atoms in blue and Zr atoms in red; the $Al_3(Sc_{1-x}Zr_x)$ precipitates are readily apparent. The dimensions of the reconstructions, the total number of atoms contained within them, and the number of $Al_3(Sc_{1-x}Zr_x)$ precipitates wholly included or intercepted by the analysis boundaries, are also indicated.

Fig. 5 displays the time-of-flight mass spectrum for the analysis reconstructed in Fig. 4b. Al has only one isotope, and the prominent Al peaks correspond to singly (Al^{1+}, 27 amu) and doubly charged (Al^{2+}, 13.5 amu) ions produced during pulsed field-evaporation. Sc is field evaporated in the doubly charged state (Sc^{2+}, 22.5 amu), whereas Zr atoms are observed in the doubly (Zr^{2+}, 45–48 amu) and triply (Zr^{3+}, 30–32 amu) charged states. Note that the Zr^{3+} peaks overlap with the Al^{1+} tail, which makes an accurate quantitative measurement of the Zr^{3+} concentration difficult.

The reconstructions in Fig. 4 indicate that both Sc and Zr partition to the $Al_3(Sc_{1-x}Zr_x)$ precipitates. This information is conveyed more quantitatively in Fig. 6, which exhibits a proximity histogram, or proxigram for short [33,34], displaying average solute concentration profiles in the α-Al matrix and $Al_3(Sc_{1-x}Zr_x)$ precipitates with respect to a constant 1.25 at.% Sc isoconcentration surface (near the inflection point in concentration profiles for all three aging treatments) delineating the two phases in all reconstructions. For the three isochronal aging temperatures

investigated, Zr is a minor constituent in the $Al_3(Sc_{1-x}Zr_x)$ precipitates, with the Zr content in the precipitates increasing with increasing aging temperatures from 0.77 ± 0.05 at.% Zr at 300 °C, to 1.86 ± 0.03 at.% Zr at 350 °C, and to 4.38 ± 0.05 at.% Zr at 400 °C. The distribution of Zr atoms in the $Al_3(Sc_{1-x}Zr_x)$ precipitates is inhomogeneous, with the precipitates generally consisting of a Zr-poor Al_3Sc core surrounded by a Zr-enriched outer shell. This core–shell solute distribution becomes more apparent with increasing aging temperature. At 300 °C, the precipitates contain a maximum of only 1.6 ± 0.4 at.% Zr, segregated near the precipitate core. After 350 °C, there is an enrichment of 2.4 ± 0.1 at.% Zr at the α-Al/$Al_3(Sc_{1-x}Zr_x)$ heterophase interface. At 400 °C, the interfacial enrichment increases significantly to 6.2 ± 0.2 at.% Zr.
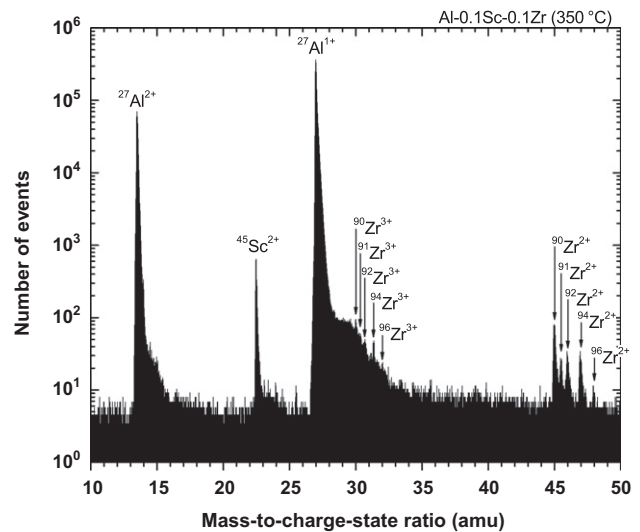
Fig. 5. LEAP tomographic mass spectrum of Al–0.1Sc–0.1Zr(a) isochronally aged to 350 °C (reconstruction shown in Fig. 4b). The post-peak Al^{1+} shoulder overlaps with the triply charged Zr^{3+}, 30–32 amu.
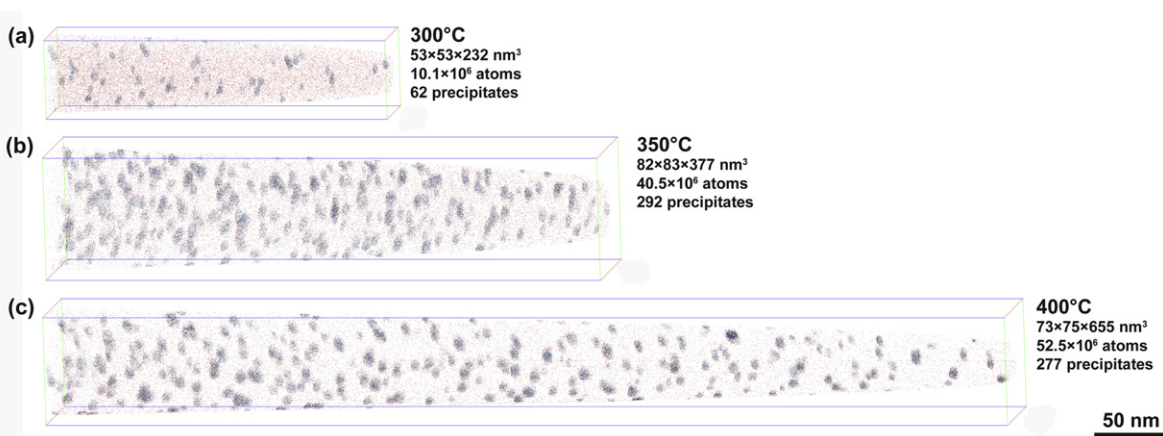
Fig. 4. Three-dimensional APT reconstructions of Al–0.1Sc–0.1Zr(a) isochronally aged to (a) 300 °C, (b) 350 °C, or (c) 400 °C. Sc atoms are shown in blue, Zr atoms are red, and the Al atoms are omitted for clarity. (For interpretation of the references to colour in this figure legend, the reader is referred to the web version of this article.)
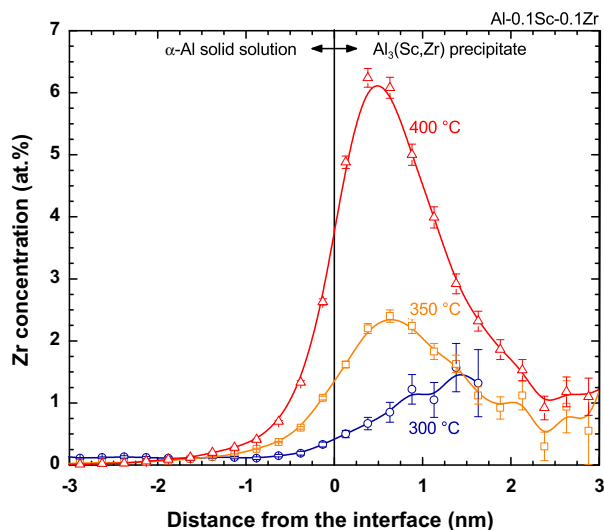
Fig. 6. Proxigrams displaying the distributions of Sc and Zr in Al₃(Sc$_{1−x}$Zr$_x$) precipitates formed in Al–0.1Sc–0.1Zr(a) isochronally aged to 300, 350 or 400 °C. Error bars are calculated employing $\sqrt{c_i(1 − c_i)/N_{tot}}$, where c_i is the atomic fraction of element i and N_{tot} is the total number of atoms in the bin.

3.5. Isothermal aging at 400 °C

To assess the stability of these alloys for extended high-temperature usage, specimens were isothermally annealed at 400 °C for 400 h, after having been isochronally aged to 400 °C. Fig. 7 displays Vickers microhardness vs. time at 400 °C for Al–0.1Sc and Al–0.1Sc–0.1Zr(a). During isochronal aging, Fig. 3, Al–0.1Sc is already overaged considerably from 668 ± 20 MPa at 325 °C, peak microhardness, to 448 ± 21 MPa at 400 °C. During further annealing at 400 °C, Fig. 7, the alloy continues to overage, with the microhardness decreasing linearly on a semilogarithmic scale to 295 ± 9 MPa after 400 h. The Al–Sc–Zr alloy also overages at 400 °C, from a near-peak microhardness of
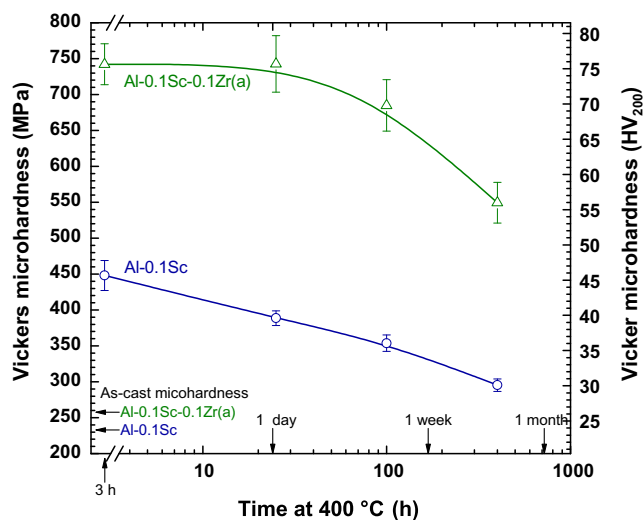

Fig. 7. Vickers microhardness vs. exposure time at 400 °C for Al–0.1Sc and Al–0.1Sc–0.1Zr (after isochronally aging to 400 °C, peak microhardness for Al–Sc–Zr).

742 ± 29 MPa to 549 ± 28 MPa after 400 h at 400 °C. Significant coarsening in Al–0.1Zr does not occur below ∼475 °C (not displayed in Fig. 6, but presented in Refs. [9,10]); it is anticipated that the microhardness after 400 h at 400 °C would be ∼370 MPa, the value obtained after the 400 °C isochronal aging treatment.

4. Discussion

4.1. As-cast microstructure

In dilute Al-based peritectic systems, for a specific cooling rate there is a corresponding critical solute concentration below which primary precipitation of Al₃M will not occur [1,43–46]. The presence of the primary precipitates in the Al–Sc–Zr alloys indicates that, for the conventional casting conditions we employed, 0.2 at.% total solute (Sc plus Zr) exceeds this critical concentration. No primary precipitates are observed in the more dilute Al–0.1Zr alloy [10], and primary Al₃Sc precipitates in Al–0.1Sc are not possible, given the eutectic composition of 0.28 at.% Sc [1,40,47,48]. This is consistent with the coarser grain structure observed in the two binary alloys.

The primary precipitation of Al₃(Sc$_{1−x}$Zr$_x$) observed in the Al–Sc–Zr alloy has several complicating consequences. The amount of solute retained in solid-solution is decreased, thus limiting the potential for precipitation strengthening during post-solidification aging. The maximum strengthening effect achieved, Fig. 3, would be significantly larger had the formation of primary Al₃(Sc$_{1−x}$Zr$_x$) been suppressed. For developing creep-resistant alloys, there is the additional challenge of the potent grain refinement effect, which results from primary precipitates acting as heterogeneous nuclei during solidification of the melt. To avoid rapid diffusional creep associated with a refined grain structure, it is necessary to reduce the solute content of the Al–Sc–Zr alloys. We have shown that primary precipitates can be suppressed during conventional solidification of more dilute Al–0.06Sc–0.06Zr alloys, producing coarse-grained castings that are suitable for creep studies [11]. The optimum composition for a creep-resistant alloy with Sc:Zr ratio of unity is thus between Al–0.06Sc–0.06Zr and Al–0.1Sc–0.1Zr.

4.2. As-cast solute microsegregation

In both regions sampled by EPMA, Fig. 2, the measured mean Sc concentration is in excellent agreement with the bulk composition (Table 1), whereas the mean Zr concentration is enriched significantly in Fig 2a. This could reflect a macrosegregation of Zr between the two 40 μm long locally sampled regions of the alloys. A similar enrichment of Zr was observed in EPMA measurements on more dilute Al–0.06Zr and Al–0.06Sc–0.06Zr alloys [11], and might also be an artifact of the EPMA technique.

Comparing the volumes analyzed by APT (∼75 × 75 × 500 nm³, Fig. 4) with the length scale of the as-cast microsegregation of Sc and Zr (∼10 μm, Fig. 2), it is apparent

that the locally measured composition of the alloy by APT can vary significantly between analyses. Within the dendritic and interdendritic regions of the as-cast alloy, Fig. 2, the Sc:Zr ratio varies from ~0.5 to ~2, respectively. Thus the local alloy composition analyzed by APT is *a priori* unknown. We could, in principle, measure the total Sc and Zr concentration within the analyzed APT volume and then deduce whether that analysis was from a Sc-poor/Zr-rich dendritic region or a Sc-rich/Zr-poor interdendritic one. However, because of the Zr^{3+} overlap with the Al^{1+} peak, Fig. 5, we cannot account accurately for all of the Zr in the analysis volume; the dilute Zr^{3+} concentrations in the α-Al solid-solution surrounding the precipitates is not measurable above the Al^{1+} tail. Furthermore there are numerous primary $Al_3(Sc_{1-x}Zr_x)$ precipitates, Fig. 1, which have scavenged some of the Sc and Zr atoms, preventing a direct comparison with the bulk concentrations in Table 1.

4.3. Vickers microhardness and electrical conductivity

The maximum increase in microhardness, Fig. 3, as compared with the value of the as-cast specimens, is 434 ± 24 MPa for Al–0.1Sc and 206 ± 12 MPa for Al–0.1Zr. Thus, on a per-atom basis, the maximum precipitation strengthening of Al–Sc is over twice that of Al–Zr. Indeed, it is known that Sc provides one of the largest increments of strengthening per atomic percent of any alloying element when added to Al [2,49]. In cast Al–Zr alloys the initial distribution of Zr solute atoms is highly nonuniform [10,11], leading to precipitate-free interdendritic channels that have a deleterious effect on ambient-temperature strength [9], which further explains the disparity in strengthening between the Al–Sc and Al–Zr alloys.

The nucleation and growth of Al_3Sc ($L1_2$) occurs at much lower temperatures than for Al_3Zr ($L1_2$), which is, in part, reflective of the disparity in diffusivities between Sc and Zr in α-Al. These diffusivities are given by an Arrhenius relationship, $D = D_0\exp(-Q/R_gT)$, where $Q = 173$ and 242 kJ mol^{-1} and $D_0 = 5.31 \times 10^{-4}$ and 7.28×10^{-2} m^2 s^{-1} for Sc and Zr, respectively [1,50,51]. At 200 °C, where precipitation of Al_3Sc is first detected (Fig. 3), the diffusivity of Sc in α-Al is 4.16×10^{-23} m^2 s^{-1}. A similar diffusivity of Zr in α-Al is achieved at 322 °C, which is somewhat comparable to the first detection of Al_3Zr precipitation occurring at 375 °C. Since precipitate growth and coarsening are diffusion-limited, the precipitation of Al_3Sc is significantly more rapid than that of Al_3Zr.

The rapid overaging of Al–0.1Sc for $T > 325$ °C is consistent with prior studies on similar conventionally solidified Al–Sc alloys, which exhibit excellent coarsening and creep resistance up to 300 °C [2–8]. The overaging of the Al–0.1Zr alloy occurs at much higher temperatures ($T > 475$ °C), which again can be explained by the relative diffusivities of Sc and Zr in α-Al. The Al–Sc alloy overages above 325 °C, where the diffusivity of Sc in α-Al is

4.10×10^{-19} m^2 s^{-1}. A comparable diffusivity for Zr occurs at 460 °C, which is in agreement with the onset of overaging above 450 °C.

The precipitation hardening behavior of both the as-cast and homogenized Al–0.1Sc specimens are identical, Fig. 3, which suggests that Sc atoms are homogeneously distributed prior to nucleation of Al_3Sc during post-solidification aging. We have measured the as-cast solute microsegregation in a similar study on more dilute Al–0.06Sc, Al–0.06Zr and Al–0.06Sc–0.06Zr alloys using EPMA [11] and found that the Sc atoms are uniformly distributed in the as-cast alloys, which reflects the fact that k_0, the equilibrium partition coefficient for solidification, is near unity for Sc ($k_0 = 0.82$ [1]). Previous studies [52–54] measuring solute microsegregation in Sc-containing commercial 7xxx alloys by EPMA also find that the degree of microsegregation of Sc atoms is relatively weak compared with other solutes (e.g. Zn, Mg, or Zr). The relatively even distribution of Sc atoms after solidification leads to a homogeneous distribution of Al_3Sc precipitates after aging, which explains why the precipitation strengthening behavior of both the as-cast and homogenized Al–Sc specimens are identical in Fig. 3.

The change in electrical conductivity between the as-cast and peak-aged conditions is 3.5 ± 0.4 MS m^{-1} for Al–0.1Sc and 3.6 ± 0.1 MS m^{-1} for Al–0.1Zr, which suggests that a similar ϕ value of precipitates is formed in both alloys, assuming that the specific resistivities of these elements are comparable. That the maximum increase in microhardness of Al–0.1Zr is less than half that of Al–0.1Sc is probably due to the deleterious effect of the precipitate-free interdendritic channels in the Al–Zr alloy [9]. In Al–0.1Sc the peak electrical conductivity, where the maximum ϕ of Al_3Sc ($L1_2$) is attained, is achieved at ~375 °C—50 °C higher than the temperature at which peak microhardness is attained. Thus the initial decline in strength from 325 to 375 °C is likely due to a change in strengthening mechanisms from order strengthening to Orowan bypass as precipitates continue to grow. The strength decrease at higher temperatures ($T > 400$ °C) is due to precipitate coarsening (Ostwald ripening) decreasing the resistance to Orowan bypass further.

The electrical conductivity of the as-cast ternary Al–0.1Sc–0.1Zr alloy is ~4 MS m^{-1} smaller than those of the binary Al–0.1Sc or Al–0.1Zr alloys, due to the larger solute additions. The maximum change in electrical conductivity from the as-cast condition should be directly related to the amount of Sc and Zr in solid-solution. This value is, however, smaller in the ternary alloy than the sum of the differences for the binary alloys. This is consistent with the primary precipitates observed in the ternary alloy, Fig. 1, which indicate that not all alloying additions are retained in solid-solution prior to aging. The microhardness of the as-cast ternary alloy is approximately 50 MPa greater than that measured for Al–0.1Sc or Al–0.1Zr. This value is also less than would be expected if all alloying contributions aided in solid-solution strengthening. In addition

to enhanced solid-solution strengthening, the finer grain size of the ternary alloy leads to Hall–Petch strengthening, $\Delta\sigma_{HP}$, given by [55,56]:

$$\Delta\sigma_{HP} = Kd^{-1/2}, \tag{1}$$

where K is the material-specific locking parameter and the grain diameter, d, is ~ 50 μm. The value of K varies as a function of alloying content [57,58] and also depends on the range in d investigated. Because the contributions of Sc and Zr on K are not known and because of the dilute concentrations of these additions, we use an average value of $K = 30$ MPa μm$^{1/2}$ for pure Al over the range 30 μm $\leqslant d \leqslant 500$ μm [59] to find $\Delta\sigma_{HP} = 4$ MPa. The increase in microhardness is three times this amount [60], or 12 MPa. Thus, Hall–Petch strengthening alone cannot account for the ~ 50 MPa increased as-cast microhardness of the Al–Sc–Zr alloys. Solid-solution strengthening must therefore also be playing a role.

For the Al–0.1Sc–0.1Zr alloys, the change in electrical conductivity between the as-cast specimens and those aged to 325 °C is 2.6 ± 0.3 MS m^{-1}, which is close to what is observed in the binary Al–0.1Sc alloy over the same temperature range (2.8 ± 0.6 MS m^{-1}), indicating that the Al$_3$(Sc$_{1-x}$Zr$_x$) precipitates formed up to 325 °C contain mainly Sc, which is consistent with the proxigrams in Fig. 6. Between 325 and 400 °C (peak strength), there is an additional change in conductivity of about 3.5 MS m^{-1}, which is similar to the change between the as-cast and peak-aged conditions in Al–0.Zr (3.6 ± 0.1 MS m^{-1}). This suggests that between 325 and 400 °C, all of the available Zr in solid-solution has precipitated out. That the peak microhardness is not achieved until 400 °C supports the APT evidence that Zr forms a shell around the Al$_3$Sc precipitates, hindering the coarsening of the Al$_3$Sc core.

4.4. Atom-probe tomography

The Zr concentration in the Al$_3$(Sc$_{1-x}$Zr$_x$) precipitates increases continuously with increasing isochronal aging temperature from 0.77 ± 0.05 at.% Zr at 300 °C to 4.38 ± 0.05 at.% Zr at 400 °C. The distribution of Zr in the Al$_3$(Sc$_{1-x}$Zr$_x$) precipitates is nonuniform, Fig. 6, with the precipitates consisting of an Al$_3$Sc core surrounded by a spherical Zr-enriched outer shell. Similar core–shell structure precipitates are well documented for Al–Sc–Zr alloys, as observed by APT [15,16,18,21], analytical high-resolution electron microscopy [17,18,61], small-angle X-ray scattering [18,62] and atomic-scale simulations [18,63]. Other systems also exhibit core–shell precipitates, as observed in APT studies on Al–Sc–Ti [64], Al–Sc–rare earth [65,66], Al–Sc–Zr–Hf [19], and Al–Li–Sc–Zr [67,68] alloys. The formation of a shell is due to a disparity in diffusivities among alloying elements, Sc and Zr in the present case. Because of the much larger diffusivity of Sc compared to Zr, only Sc atoms are kinetically able to participate in the early stages of nucleation and growth. These pre-existing precipitates then act as heterogeneous nucleation sites for the less-mobile Zr atoms, which form shells on the Al$_3$Sc precipitates rather than nucleating new Al$_3$Zr precipitates.

The APT data in Fig. 4 were used to determine $\langle R \rangle$, ϕ and N_v of the Al$_3$(Sc$_{1-x}$Zr$_x$) precipitates directly in three dimensions. The radius, R, of an individual precipitate containing n atoms in the reconstruction is equated to the radius of the volume equivalent sphere:

$$R = \left(\frac{3}{4\pi} \frac{n\Omega}{\eta} \right)^{1/3}, \tag{2}$$

where Ω is the theoretical atomic volume and η is the estimated detection efficiency of 0.5 for the LEAP tomograph's multichannel plate detector. The atomic volume is calculated using $\Omega = a^3/4$, where a is the precipitate lattice parameter and the factor 4 represents the number of atoms in an ordered fcc (L1$_2$) unit cell. The lattice parameter of Al$_3$(Sc$_{1-x}$Zr$_x$) (L1$_2$) is proportional to x, varying from 0.4103 nm for $x = 0$, to 0.4092 nm for $x = 0.5$ [14].

For each aging temperature, the average of the measured precipitate compositions was used to determine Ω. The number of atoms, n, contained in each precipitate was determined by taking the contents of an isoconcentration surface whose value is that of the inflection point of the Sc concentration profile in the proxigram (~ 3 at.% Sc) [33,34]. Due to the strong partitioning of Sc to the precipitates, the calculated R is insensitive to the exact concentration chosen for this surface. The R value found by this method is also consistent with that found by using the envelope method [35,36]. The precipitate volume fraction, ϕ, is determined directly from the ratio of the total number of atoms contained within the precipitates to the total number of atoms collected and the average atomic density of the two phases, as calculated from their respective lattice parameters ($a = 0.40496$ nm for Al [1]). The number density, N_v, is calculated directly from the number of precipitates in the analyzed volume. For the purpose of measuring both $\langle R \rangle$ and N_v, precipitates fully contained in the reconstruction volume are counted as whole precipitates and those that are cut by the surface of the reconstructed volume are counted as half precipitates [36]. The difference in $\langle R \rangle$ between precipitates counted as whole and half is less than one standard deviation of the precipitate radius, and is $\sim 10\%$ for all measured data sets. This systematic error arises from the minimum detectable precipitate size preventing some precipitates that are cut by the analysis boundary from being measured. The measured $\langle R \rangle$, ϕ, and N_v values of the Al$_3$(Sc$_{1-x}$Zr$_x$) precipitates aged isochronally to 300, 350 or 400 °C are presented in Table 2.

The values of $\langle R \rangle$ and ϕ increase substantially between 300 and 350 °C, as both Sc and Zr atoms continue to precipitate out onto the growing precipitates. Microsegregation (the alloys were not homogenized) and the small changes compared with measurement uncertainty may both explain why we do not observe a monotonic increase in $\langle R \rangle$ and ϕ between 350 and 400 °C that we would expect based on the electrical conductivity results. The value of N_v remains of the same order of magnitude, changing by less

Table 2
Measured mean precipitate radii, $\langle R \rangle$, precipitate volume fraction, ϕ, and number density, N_v, for $Al_3(Sc_{1-x}Zr_x)$ precipitates in Al–0.1Sc–0.1Zr isochronally aged to 300, 350 or 400 °C.

T (°C)	$\langle R \rangle$ (nm)	ϕ (%)	$N_v \times 10^{23}$ m^{-3}
300	1.5 ± 0.6	0.30 ± 0.01	1.5 ± 0.2
350	1.9 ± 0.8	0.50 ± 0.03	1.7 ± 0.1
400	1.7 ± 0.7	0.44 ± 0.03	1.33 ± 0.09

than 25%, for the three aging conditions studied by APT. This is expected during this stage of isochronal aging, as precipitates nucleated at earlier aging treatments act as heterogeneous nuclei for solute atoms still in solid-solution. Thus, the precipitation of Sc and Zr from 300 to 400 °C contributes primarily to the growth of the $Al_3(Sc_{1-x}Zr_x)$ precipitates rather than to new precipitate nucleation. The small variation in N_v also indicates that there is negligible precipitate coarsening for these aging treatments up to 400 °C.

We now compare our results to prior APT studies on Al–Sc–Zr alloys. Some studies have a comparable Sc content, but all have a smaller Zr concentration and employ greater aging temperatures and times. Forbord et al. [16] aged an Al–0.09Sc–0.02Zr alloy at 475 °C for 15 h. Their higher aging temperature as compared with ours resulted in larger $Al_3(Sc_{1-x}Zr_x)$ precipitates ($\langle R \rangle = 9.6$ nm, as measured by transmission electron microscopy (TEM)) containing more Zr (4.5 at.%), despite their smaller Zr:Sc ratio. The core–shell structure was, however, retained, as they observed an ~8 nm thick Zr-rich shell surrounding an ~2.5 nm radius Sc-rich core. Clouet et al. [18] studied a similar Al–0.09Sc–0.03Zr alloy aged for a longer time (128 h) at the same maximum temperature we have analyzed by LEAP tomography (400 °C), and observed a 12 at.% Zr enrichment at the α-Al/$Al_3(Sc_{1-x}Zr_x)$ heterophase interface. This interfacial enrichment is larger than what we observed (6.2 ± 0.2 at.% Zr) after 3 h at 400 °C, despite the smaller Zr:Sc ratio in their alloy [18]. Utilizing high-angle annular dark-field TEM for alloys aged for 32 h at 450 °C, Clouet et al. [18] also observed a 2–4 nm thick Zr-rich shell containing about 12 at.% Zr surrounding a $\langle R \rangle \sim 10$ nm Sc-rich core. Fuller et al. [15,69] aged an Al–0.09Sc–0.05Zr alloy isothermally at 300 °C, and observed via APT that the Zr in the precipitates increased from 0.4 at.% after 4.5 h (comparable to the amount we measured at this temperature) to 1.2 at.% after 2412 h (less than the amount that we measured at 400 °C). The precipitates in their study were of a comparable size to ours ($\langle R \rangle \sim 2$ nm) for the extended aging treatments at 300 °C. There was, however, significant precipitate coarsening after isothermal aging at 350 or 375 °C for at least 10 h. The small $\langle R \rangle$ and increasing ϕ values that we have measured indicate that isochronal heat treatments may be effective at optimizing alloy strength in a short time. The results of Fuller et al. suggest, however, that longer annealing at temperatures greater than 300 °C will reduce this strength.

4.4.1. Precipitation strengthening in Al–Sc–Zr alloys

Fig. 3 demonstrates that the observed strength increase (as compared with the value of the as-cast, unaged specimens) for the Al–0.1Sc–0.1Zr(a) alloy is $\Delta\sigma = 131 \pm 11$, 161 ± 15 and 162 ± 10 MPa at 300, 350 and 400 °C, respectively, using a conversion factor of $\frac{1}{3}$ between Vickers microhardness and strength [60]. The results in Fig. 6 indicate that this strength increase is attributable to segregation of Zr to pre-existing Al_3Sc precipitates, effectively increasing ϕ of the precipitates without diminishing N_v, thereby increasing the yield stress of the alloy.

Theories of precipitation strengthening have been reviewed in Refs. [70–75]. Precipitate shearing, precipitate bypass by dislocation looping, or a combination of these two mechanisms can generally explain ambient-temperature strength in precipitate-strengthened alloys in the absence of other strengthening mechanisms (e.g. Hall–Petch strengthening, solid-solution strengthening or strain hardening).

For coherent precipitates with small R, the strength is controlled by dislocations shearing precipitates, as observed experimentally for Al–Sc [7,8] and Al–Li [76,77] alloys. The small ($\langle R \rangle < 2$ nm) precipitates we observe are expected to be fully coherent, since Al_3Sc precipitates are coherent to at least $\langle R \rangle = 15$ nm [6,13,49,78–80]. In addition, Zr reduces the lattice parameter mismatch of $Al_3(Sc_{1-x}Zr_x)$ with α-Al [14,81], further increasing the critical radius at which coherency is lost. For the shearing mechanism, the increase in yield strength results from three contributions: (i) modulus mismatch strengthening; (ii) coherency strengthening; and (iii) order strengthening.

First, the strengthening due to modulus mismatch, $\Delta\sigma_{ms}$, results from differences in the shear moduli of the precipitate and matrix phases and is given by [71]:

$$\Delta\sigma_{ms} = M \cdot 0.0055(\Delta G)^{3/2}\left(\frac{\phi}{\Gamma}\right)^{1/2} b\left(\frac{\langle R \rangle}{b}\right)^{3m/2-1}, \quad (3)$$

where $M = 3.06$ is the Taylor mean orientation factor [82], ΔG is the difference in the shear modulus between the matrix and precipitate, $\Gamma = \frac{1}{2}G_{Al}b^2$ is the line tension of the dislocation in Al, $b = 0.286$ nm is the magnitude of the Al Burgers vector [83], and $m = 0.85$ is a constant [71]. The shear modulus of the $Al_3(Sc_{1-x}Zr_x)$ precipitates is taken to be $G_{Al_3(Sc_x Zr_{1-x})} = 68$ GPa, which is the value for Al_3Sc ($L1_2$) [84–86] and also Fe-stabilized Al_3Zr ($L1_2$) [87–89]. The shear modulus of the Al matrix is $G_{Al} = 25.4$ GPa [83].

Second, coherency strengthening, $\Delta\sigma_{cs}$, arises through the elastic strain–field interactions between coherent precipitates and dislocations, and is given by [71]:

$$\Delta\sigma_{cs} = M \cdot \chi(\epsilon G_{Al})^{3/2}\left(\frac{\langle R \rangle \phi b}{\Gamma}\right)^{1/2}, \quad (4)$$

where $\chi = 2.6$ [71], ϵ is a mismatch parameter approximated by $\frac{2}{3}\delta$; $\delta = 1.3\%$ is the lattice parameter mismatch for the $Al_3(Sc_{1-x}Zr_x)$ precipitates estimated from the com-

position-dependent lattice parameters [14,90]. Coherency strengthening occurs in parallel with modulus mismatch strengthening.

Third, order strengthening, $\Delta\sigma_{os}$, is due to the formation of antiphase boundaries (APBs), which occurs when matrix dislocations shear ordered precipitates. At peak strength, $\Delta\sigma_{os}$ is given by [71,74]:

$$\Delta\sigma_{os} = M \cdot 0.81 \frac{\gamma_{APB}}{2b} \left(\frac{3\pi\phi}{8}\right)^{1/2}, \qquad (5)$$

where $\gamma_{APB} \sim 0.5\,\mathrm{J\,m^{-2}}$ is an average value of the Al$_3$Sc APB energy for the (1 1 1) plane taken from several reported values [84,86–88,91]. Because order strengthening acts serially to coherency and modulus mismatch strengthening, the alloy shear strength increment due to precipitate shearing is determined as the maximum value of $\Delta\sigma_{ms} + \Delta\sigma_{cs}$ and $\Delta\sigma_{os}$.

As $\langle R \rangle$ increases, the theoretical shear strength of precipitates increases accordingly, until strength becomes controlled by another mechanism, Orowan dislocation looping, which is given by [92]:

$$\Delta\sigma_{or} = M \cdot \frac{0.4 \cdot G_{Al} \cdot b}{\pi\sqrt{1-v}} \cdot \frac{\ln\left(\frac{2\bar{R}}{b}\right)}{\lambda_{e-e}}, \qquad (6)$$

where $v = 0.345$ is Poisson's ratio [82] for Al. For a monodispersed population of precipitates, the mean planar radius is $\bar{R} = \frac{\pi}{4}\langle R \rangle$, and the edge-to-edge interprecipitate spacing is $\lambda_{e-e} = \left(\sqrt{\frac{2\pi}{3\phi}} - \frac{\pi}{2}\right)\langle R \rangle$ [71,73,74]; these equations are also valid for polydispersed arrays [74].

Fig. 8 displays the theoretical and measured strength increases of isochronally aged Al–0.1Sc–0.1Zr(a) as a function of $\langle R \rangle$. For all three aging temperatures the small $\langle R \rangle$ values predict an Orowan strengthening increment that is much larger than the calculated precipitate shear strength. The precipitates are therefore shearable, although the mechanism of shear resistance is debatable. While $\Delta\sigma_{os}$ is in excellent agreement with measured values, the sum $\Delta\sigma_{cs} + \Delta\sigma_{ms}$ is still within error of the propagated uncertainty in the $\langle R \rangle$ and ϕ values. In other Al–Sc–X alloys, strengthening that is nearly independent of $\langle R \rangle$ has been observed (as is predicted by $\Delta\sigma_{os}$), rather than the dependence that is predicted from $\Delta\sigma_{cs} + \Delta\sigma_{ms}$ [7,8,93]. The present alloys are microsegregated, Fig. 2, which will probably introduce variations in $\langle R \rangle$ and precipitate composition associated with the nonuniform Sc:Zr ratio and solute supersaturations. The precipitate measurements from APT analysis volumes span ∼100 nm, while each microhardness indent is ∼100 μm. If there is a wide variation in $\langle R \rangle$ from microsegregation of solutes, then the excellent agreement in Fig. 8 between the theoretical and measured strength increases may be fortuitous.

The simplification that the precipitate shear strength is determined by the maximum of one of the two serial processes may not be valid. Alternatively, our estimation of $\Delta\sigma_{cs} + \Delta\sigma_{ms}$ is too large, but this does not seem likely
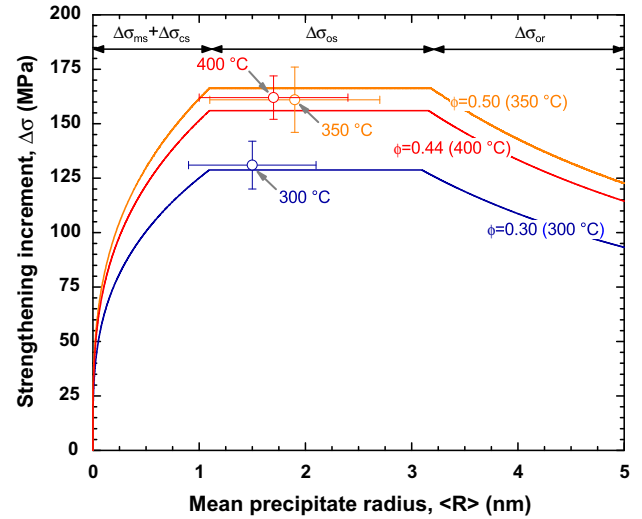

Fig. 8. Yield stress increment vs. mean precipitate radius, $\langle R \rangle$, for Al–0.1Sc–0.1Zr(a) isochronally aged to 300, 350 or 400 °C. The curves represent calculated predictions of the minimum of $\Delta\sigma_{ms} + \Delta\sigma_{cs}$ (Eqs. (3) and (4)), $\Delta\sigma_{os}$ (Eq. (5)), and $\Delta\sigma_{or}$ (Eq. (6)). The symbols represent the yield stress calculated from Vickers microhardness measurements.

because the precipitates are expected to remain coherent at this very small size, and, while there is some variation in the reported values of γ_{APB}, the value employed is in agreement with TEM measurements of dislocation spacings [7,8], and our calculated values of $\Delta\sigma_{os}$ have much less propagated uncertainty than $\Delta\sigma_{cs} + \Delta\sigma_{ms}$ because there is no $\langle R \rangle$ dependence. Thus, we propose that order strengthening is the controlling strengthening mechanism for these three heat treatments.

These results are in agreement with prior results on Al–0.18Sc [7,8] and several Al–Sc–Zr alloys [90], for which Orowan dislocation looping is the main strengthening mechanism only for $\langle R \rangle > 2$ nm, while smaller precipitates are shearable. In Refs. [7,8], we note that strengthening increments much lower than those predicted by $\Delta\sigma_{cs} + \Delta\sigma_{ms}$ may be due to simultaneous bypass of precipitates by shear and Orowan looping. Because of the large volume of the present datasets and the small $\langle R \rangle$ values leading to nearly maximum theoretical strength (for a given ϕ), we are presently using these reconstructions in dislocation dynamics simulations [94,95] that may provide insight into this hypothesis.

4.5. Isothermal aging at 400 °C

While the Al–Sc–Zr alloys reach peak microhardness at 400 °C during isochronal aging, Fig. 3, the Al$_3$(Sc$_{1-x}$Zr$_x$) precipitates undergo coarsening after extended time (starting at 100 h and pronounced at 400 h) at this temperature, Fig. 7. The decrease in microhardness observed at 400 °C is consistent with prior studies on Al–Sc–Zr alloys aged isothermally at 300–500 °C. Elagin et al. [4] investigated an Al–0.24Sc–0.05Zr alloy during isothermal aging at 300–500 °C, and first observed a measurable decrease in

microhardness after 278 h at 400 °C. Davydov et al. [96] investigated an Al–0.12Sc–0.04Zr alloy and observed negligible coarsening up to 278 h at 400 °C, but significant coarsening beyond 4 h at 450 °C. Thus, the threshold for long-term stability of $Al_3(Sc_{1-x}Zr_x)$ seems to be ~400 °C. Nevertheless, Al–0.1Sc–0.1Zr is still stronger after 400 h at 400 °C than any other conventionally cast Al alloy known to the authors.

5. Conclusions

Precipitation of Al_3Sc, Al_3Zr, and $Al_3(Sc_{1-x}Zr_x)$ (L1$_2$) precipitates has been investigated in conventionally solidified Al–0.1Sc, Al–0.1Zr and Al–0.1Sc–0.1Zr (at.%) alloys, isochronally aged from 200 to 600 °C. The following results are obtained:

- The as-cast microstructure of the binary Al–0.1Sc and Al–0.1Zr alloys is typical of conventionally cast alloys, with large (millimeter-scale) columnar grains without primary Al_3Sc or Al_3Zr precipitates. The Al–0.1Sc–0.1Zr alloy has fine (~50 μm) equiaxed grains, which are the result of $Al_3(Sc_{1-x}Zr_x)$ primary precipitates acting as grain refiners during solidification. Because these primary precipitates reduce the potential for precipitation hardening during post-solidification aging, the total (Sc plus Zr) solute content should be below 0.2 at.% in conventionally cast alloys if ambient and creep strength are to be optimized.
- In the as-cast Al–0.1Sc–0.1Zr alloy, Sc is concentrated at the dendrite peripheries, while Zr is microsegregated at the dendrite cores, as measured by EPMA. The degree of Zr microsegregation is more pronounced than that of Sc.
- Precipitation of Al_3Sc (L1$_2$) commences between 200 and 250 °C in the Al–0.1Sc alloy, reaching a peak microhardness of 668 ± 20 MPa at 325 °C. In the Al–0.1Zr alloy, precipitation of Al_3Zr (L1$_2$) commences between 350 and 375 °C, achieving a peak microhardness of 420 MPa at 425–450 °C. Sc diffuses much more rapidly than Zr at these temperatures, which explains the faster precipitation kinetics for the Al–Sc alloy. On a per-atom basis, Sc is a significantly more potent strengthener than Zr, probably because of the nonuniform precipitate distributions in the Al–Zr alloys (Fig. 1), which are known to be deleterious to the mechanical properties [9].
- In the Al–0.1Sc–0.1Zr alloy, the precipitation hardening behavior follows that of Al–0.1Sc up to 325 °C. Beyond this temperature, Zr additions result in a secondary increase in strength, attaining a peak Vickers microhardness of 782 ± 37 MPa at 400 °C. Overaging is delayed in Al–0.1Sc–0.1Zr by more than 100 °C compared with the Zr-free alloy.
- The average Zr concentration in the $Al_3(Sc_{1-x}Zr_x)$ precipitates, as measured by APT, increases continuously with increasing isochronal aging temperature. At 300 °C the precipitates contain 0.77 ± 0.05 at.% Zr; at 350 °C they contain 1.86 ± 0.03 at.% Zr; and at 400 °C they contain 4.38 ± 0.05 at.% Zr. Zr segregates to the α-Al/$Al_3(Sc_{1-x}Zr_x)$ heterophase interface, forming a Zr-enriched outer shell surrounding the Al_3Sc precipitates, thereby increasing the precipitate volume fraction, ϕ, from ~0.3% to ~0.5%. The precipitates remain small ($\langle R \rangle < 2$ nm) and the number density remains large ($N_v \sim 10^{23}$ m^{-3}) and the increase in the yield stress of the alloy, by ~30 MPa, results from an increase in the alloy shear strength increment due to precipitate shearing.
- While the Al–0.1Sc–0.1Zr alloy achieves peak microhardness after isochronal aging to 400 °C, it overages after extended annealing at this temperature, Fig. 7, indicating that it is not suitable for extended use at 400 °C.

References

[1] Knipling KE, Dunand DC, Seidman DN. Z Metallkd 2006;97:246–65.
[2] Drits MY, Ber LB, Bykov YG, Toropova LS, Anastasyeva GK. Phys Met Metall 1984;57:118–26.
[3] Drits MY, Dutkiewicz J, Toropova LS, Salawa J. Cryst Res Technol 1984;19:1325–30.
[4] Elagin V, Zakharov V, Pavlenko S, Rostova T. Phys Met Metall 1985;60:88–92.
[5] Fuller CB, Seidman DN, Dunand DC. Scripta Mater 1999;40:691–6.
[6] Marquis EA, Seidman DN. Acta Mater 2001;49:1909–19.
[7] Seidman DN, Marquis EA, Dunand DC. Acta Mater 2002;50:4021–35.
[8] Marquis EA, Seidman DN, Dunand DC. Acta Mater 2003;51:285–7.
[9] Knipling KE, Dunand DC, Seidman DN. Acta Mater 2008;56:1182–95.
[10] Knipling KE, Dunand DC, Seidman DN. Acta Mater 2008;56:114–27.
[11] Knipling KE, Seidman DN, Dunand DC. Acta Mater, submitted for publication.
[12] Knipling KE, Dunand DC. Scripta Mater 2008;59:387–90.
[13] Toropova LS, Eskin D, Kharakterova M, Dobatkina T. Advanced aluminum alloys containing scandium: structure and properties. Amsterdam: Gordon & Breach; 1998.
[14] Harada Y, Dunand DC. Mater Sci Eng A 2002;329–331:686–95.
[15] Fuller CB, Murray JL, Seidman DN. Acta Mater 2005;53:5401–13.
[16] Forbord B, Lefebvre W, Danoix F, Hallem H, Marthinsen K. Scripta Mater 2004;51:333–7.
[17] Tolley A, Radmilovic V, Dahmen U. Scripta Mater 2005;52:621–5.

[18] Clouet E, Lae L, Epicier T, Lefebvre W, Nastar M, Deschamps A. Nat Mater 2006;5:482–8.
[19] Hallem H, Lefebvre W, Forbord B, Danoix F, Marthinsen K. Mater Sci Eng A 2006;421:154–60.
[20] Belov NA, Alabin AN, Eskin DG, Istomin-Kastrovskii VV. J Mater Sci 2006;41:5890–9.
[21] Lefebvre W, Danoix F, Hallem H, Forbord B, Bostel A, Marthinsen K. J Alloys Compd 2009;470:107–10.
[22] Vlach M, Stulíková I, Smola B, Zaludova N, Cerna J. J Alloys Compd 2010;492:143–8.
[23] Fujikawa SI, Sugaya M, Takei H, Hirano K. J Less-Common Met 1979;63:87–97.
[24] Rosen M. Metall Trans A 1989;20:605–10.
[25] Jo HH, Fujikawa SI. Mater Sci Eng A 1993;171:151–61.
[26] Royset J, Ryum N. Mater Sci Eng A 2005;396:409–22.
[27] Clouet E, Barbu A. Acta Mater 2007;55:391–400.
[28] Kelly TF, Camus P, Larson DJ, Holzman L, Bajikar S. Ultramicroscopy 1996;62:29–42.
[29] Kelly TF, Larson DJ. Mater Charact 2000;44:59–85.
[30] Kelly TF, Gribb T, Olson J, Martens R, Shepard J, Wiener SA, et al. Microsc Microanal 2004;10:373–83.
[31] Kelly TF, Miller MK. Rev Sci Instrum 2007;78:031101.
[32] Seidman DN. Ann Rev Mater Res 2007;37:127–58.
[33] Hellman OC, Vandenbroucke J, Rusing J, Isheim D, Seidman DN. Microsc Microanal 2000;6:437–44.
[34] Hellman OC, Seidman DN. Mater Sci Eng A 2002;327:24–8.
[35] Miller MK. Atom probe tomography: analysis at the atomic level. New York: Plenum; 2000.
[36] Miller MK, Kenik EA. Microsc Microanal 2004;10:336–41.
[37] Marquis EA, Seidman DN, Dunand DC. Acta Mater 2003;51:4751–60.
[38] Ohashi T, Ichikawa R. Z Metallkd 1973;64:517–21.
[39] Dahl W, Gruhl W, Burchard WG, Ibe G, Dumitrescu C. Z Metallkd 1977;68:121–7.
[40] Norman AF, Prangnell P, McEwen R. Acta Mater 1998;46:5715–32.
[41] Hyde KB, Norman AF, Prangnell PB. Mater Sci Forum 2000;331–333:1013–8.
[42] Hyde K, Norman AF, Prangnell P. Acta Mater 2001;49:1327–37.
[43] Kerr HW, Cisse J, Bolling GF. Acta Metall 1974;22:677–86.
[44] Kerr HW, Kurz W. Int Mater Rev 1996;41:129–64.
[45] St John DH, Hogan LM. J Mater Sci 1982;17:2413–8.
[46] Knipling KE, Dunand DC, Seidman DN. Metall Mater Trans A 2007;38:2552–63.
[47] Murray JL. J Phase Equil 1998;19:380–4.
[48] Okamoto H. Phase diagrams of dilute binary alloys. Materials Park: ASM International; 2002.
[49] Royset J, Ryum N. Int Mater Rev 2005;50:19–44.
[50] Fujikawa SI. Defect Diffus Forum 1997;143–147:115–20.
[51] Marumo T, Fujikawa S, Hirano K. J Jpn Inst Light Metals 1973;23:17–25.
[52] Costello FA, Robson JD, Prangnell PB. Mater Sci Forum 2002;396–402:757–62.
[53] Forbord B, Hallem H, Marthinsen K. In: Nie JF, Morton AJ, Muddle BC, editors. Proceedings of the ninth international conference on aluminium alloys. North Melbourne: Institute of Materials Engineering Australasia Ltd; 2004. p. 1179–85.
[54] Robson J. Acta Mater 2004;52:1409–21.
[55] Hall EO. Proc Phys Soc B 1951;64:747–53.
[56] Petch NJ. J Iron Steel Inst 1953;174:25–8.
[57] Witkin D, Lavernia E. Prog Mater Sci 2006;51:1–60.
[58] Ramesh K. Nanomaterials: mechanics and mechanisms. Boston: Springer Verlag; 2009.
[59] Sato YS, Urata M, Kokawa H, Ikeda K. Mater Sci Eng A 2003;354:298–305.
[60] Tabor D. Br J Appl Phys 1956;7:159–66.
[61] Iwamura S, Miura Y. J Jpn Inst Light Metals 2006;56:100–4.
[62] Deschamps A, Lae L, Guyot P. Acta Mater 2007;55:2775–83.
[63] Clouet E, Nastar M, Barbu A, Sigli C, Martin G. In: Howe JM, Laughlin DE, Lee JK, Dahmen U, Soffa WA, editors. Solid–solid phase transformations in inorganic materials. Warrendale: TMS; 2005. p. 683–703.
[64] van Dalen ME, Dunand DC, Seidman DN. Acta Mater 2005;53:4225–35.
[65] Karnesky RA, van Dalen ME, Dunand DC, Seidman DN. Scripta Mater 2006;55:437–40.
[66] Karnesky RA, Dunand DC, Seidman DN. Acta Mater 2009;57:4022–31.
[67] Radmilovic V, Tolley A, Marquis EA, Rossell MD, Lee Z, Dahmen U. Scripta Mater 2008;58:529–32.
[68] Krug M, Dunand D, Seidman D. Appl Phys Lett 2008;92. 12410 7:1–3.
[69] Fuller CB, Seidman DN. Acta Mater 2005;53:5415–28.
[70] Decker RF. Metall Trans 1973;4:2495–518.
[71] Ardell AJ. Metall Trans A 1985;16:2131–65.
[72] Martin JW. Micromechanisms in particle hardened alloys. Cambridge: Cambridge University Press; 1980.
[73] Nembach E. Particle strengthening of metals and alloys. New York: John Wiley; 1997.
[74] Ardell A. In: Westbrook JH, Fleischer RL, editors. Intermetallic compounds: principles and practice, vol. 2. Chichester: John Wiley; 1994. p. 257–86.
[75] Martin JW. Precipitation hardening. 2nd ed. Boston: Butterworth-Heinemann; 1998.
[76] Jeon SM, Park JK. Philos Mag A 1994;70:493–504.
[77] Jeon SM, Park JK. Acta Mater 1996;44:1449–55.
[78] Iwamura S, Miura Y. Acta Mater 2004;52:591–600.
[79] Røyset J, Ryum N. Scripta Mater 2005;52:1275–9.
[80] Tsivoulas D, Robson JD. Mater Sci Forum 2006;519–521:473–8.
[81] Harada Y, Dunand DC. Scripta Mater 2003;48:219–22.
[82] Meyers MA, Chawla KK. Mechanical metallurgy: principles and applications. Englewood Cliffs: Prentice Hall; 1984.
[83] Frost HJ, Ashby MF. Deformation-mechanism maps: the plasticity and creep of metals and ceramics. New York: Pergamon Press; 1982.
[84] Fu CL. J Mater Res 1990;5:971–9.
[85] Hyland Jr RW, Stiffler RC. Scripta Metall Mater 1991;25:473–7.
[86] Fu CL, Yoo MH. Mater Chem Phys 1992;32:25–36.
[87] George EP, Horton JA, Porter WD, Schneibel JH. J Mater Res 1990;5:1639–48.
[88] George EP, Pope DP, Fu CL, Schneibel JH. ISIJ Int 1991;31:1063–75.
[89] Kumar KS. In: Stoloff NS, Sikka VK, editors. Physical metallurgy and processing of intermetallic compounds. London: Chapman & Hall; 1996. p. 92–440.
[90] Fuller CB, Seidman DN, Dunand DC. Acta Mater 2003;51:4803–14.
[91] Fukunaga K, Shouji T, Miura Y. Mater Sci Eng A 1997;239–240:202–5.
[92] Hirsch P, Humphreys F. In: Argon AS, editor. Physics of strength and plasticity. Cambridge: MIT Press; 1969. p. 189–216.
[93] Karnesky RA. PhD thesis, Northwestern University; 2007.
[94] Karnesky RA, Isheim D, Seidman DN. Appl Phys Lett 2007;91. 013111 :1–3.
[95] Mohles V. Mater Sci Eng A 2004;365:144–50.
[96] Davydov V, Elagin V, Zakharov V, Rostova T. Met Sci Heat Treat 1996;38:347–52.